Lab on a Chip

PAPER

View Article Online
View Journal | View Issue

Cite this: *Lab Chip*, 2023, **23**, 2286

Lab-in-a-fiber-based integrated particle separation and counting†

T. Kumar, ‡[a] A. V. Harish, ‡[b] S. Etcheverry,[c] W. Margulis,[c] F. Laurell[b] and A. Russom *[ad]

Received 22nd December 2022,
Accepted 5th April 2023

DOI: 10.1039/d2lc01175a

rsc.li/loc

An all-fiber integrated device capable of separating and counting particles is presented. A sequence of silica fiber capillaries with various diameters and longitudinal cavities are used to fabricate the component for size-based elasto-inertial passive separation of particles followed by detection in an uninterrupted continuous flow. Experimentally, fluorescent particles of 1 μm and 10 μm sizes are mixed in a visco-elastic fluid and fed into the all-fiber separation component. The particles are sheathed by an elasticity enhancer (PEO – polyethylene oxide) to the side walls. Larger 10 μm particles migrate to the center of the silica capillary due to the combined inertial lift force and elastic force, while the smaller 1 μm particles are unaffected, and exit from a side capillary. A separation efficiency of 100% for the 10 μm and 97% for the 1 μm particles is achieved at a total flow rate of 50 μL min^{-1}. To the best of our knowledge, this is the first time effective inertial-based separation has been demonstrated in circular cross-section microchannels. In the following step, the separated 10 μm particles are routed through another all-fiber component for counting and a counting throughput of ~1400 particles per min is demonstrated. We anticipate the ability to combine high throughput separation and precise 3D control of particle position for ease of counting will aid in the development of advanced microflow cytometers capable of particle separation and quantification for various biomedical applications.

Introduction

Continuous separation of particles and cells is a prerequisite in many biomedical research areas. For instance, in biological assays, the isolation of a pure cell population from a complex biological sample is an important preparatory step before downstream analysis. Several conventional methods exist for this purpose, including fluorescent-activated cell sorters (FACS) and magnetic-activated cell sorters (MACS). However, these systems are costly and are often limited to equipped laboratories. In addition, FACS often require preparatory steps for complex samples, such as blood.

The ability to manipulate particles precisely has attracted considerable interest in the field of microfluidics. Fueled by the drive towards miniaturization and integration, microfluidic technology has emerged as an alternative to improve upon conventional separation techniques. Microfluidics technology allows for the fabrication of miniature devices at low cost, opening the possibility of point-of-care (POC) diagnosis.[1] Microfluidic methods separate cells based on their physical, chemical, and functional properties for high throughput cell separation.[2] Microfluid-based cell separation has been demonstrated using affinity biomarkers[3–5] with active techniques such as magnetic[6–8] and acoustic separation,[9–12] and by passive techniques such as deterministic lateral displacement (DLD),[13–15] inertial[16–20] and elasto-inertial microfluidics.[21–26] The latter two show simplicity, high throughput, the capability of processing huge volumes of samples, and low stress on cells. Inertial microfluidics relies on inertial forces that act on the flowing particles or cells at a high flow rate through a microfluidic channel. Depending on the geometry of the channel, these forces drive the particles to a specific streamlined position, allowing for particle focusing or separation from a mixed population.

The initial experiential work on inertial microfluidics dates back more than 50 years when Segré and Silberberg

[a] *Division of Nanobiotechnology, Department of Protein Science, Science for life laboratory, KTH Royal Institute of Technology, Solna, Sweden.*
E-mail: aman@kth.se
[b] *Laser Physics, Department of Applied Physics, KTH Royal Institute of Technology, Stockholm, Sweden*
[c] *Research Institutes of Sweden (RISE), Stockholm, Sweden*
[d] *AIMES - Center for the Advancement of Integrated Medical and Engineering Sciences at Karolinska Institutet and KTH Royal Institute of Technology, Stockholm, Sweden*

† Electronic supplementary information (ESI) available. See DOI: https://doi.org/10.1039/d2lc01175a

‡ Authors contributed equally.

observed that particles flowing through circular pipes were arranged in the annulus centered at 0.3 times the diameter of the centimeter-scale pipe cross-section.[27] With the evolution of microfabrication and rapid prototyping techniques, flow through rectangular cross-sections with straight or curved channel geometries, has made inertial microfluidics an attractive particle focusing and separation technique.[28,29] Inertial focusing in microfluidics relies on the balance between shear-lift and wall-interaction forces present in fluids at relatively high Reynolds numbers ~1–100. In recent years, elasto-inertial microfluidics (flows in non-Newtonian fluids) has become an interesting alternative to inertial microfluidics as it has the potential for single-stream 3D focusing and higher separation efficiency, especially for smaller particles.[25] Elasto-inertial microfluidics combines the inertial forces with additional viscoelastic forces that occur when using non-Newtonian fluids.[30] This allows extending the applicability of inertial microfluidics by covering a larger range of particle sizes and channel geometries. In visco-elastic fluid flows dominant lift force (F_L) and elastic force (F_E) are harnessed to provide the unique advantage of single-stream particle focusing in a straight channel. The importance of these forces is gauged by two critical dimensionless numbers: the Reynolds (Re) and Weissenberg (Wi) numbers. Re, quantifying the importance of inertia over viscous effects, is defined as $\mathrm{Re} = \rho U_c H/\mu$, where ρ is the fluid density, U_c the centreline flow velocity, H the characteristic length across the microfluidic channel cross-section, and μ is the shear viscosity of the fluid. The Weissenberg number is defined as $\mathrm{Wi} = \lambda U_c/H$, where λ is the relaxation time of the polymer additives to the fluid.

Significant progress has been made in microfluidic-based cell separation.[31,32] However, a miniaturized device for cell analysis in a POC setting should include, besides cell separation, the capability of detecting and counting the cells.[33] To date, microfluidic devices for cell separation mostly rely on external bulky flow cytometers, coulter counters, or microscopes for detection, which increases the overall size and cost of the devices and prevents their use in POC settings. On the other hand, integrated and miniaturized flow cytometers have been demonstrated by using waveguides or embedded optical fibers,[30,34] but they lack the capability of separating the cells of interest from the sample.

Fiber microfluidics offers several advantages over planar microfluidics in therapy and medical diagnostics.[35,36] Fiber optics is often used in imaging (endoscopes), biosensing, and optical coherence tomography. Fiber drawing techniques allow for the fabrication of kilometer-length of high-quality silica microstructured fiber structures at low cost. The cylindrical geometry of the optical fiber capillaries where the diameter of the cavities ranges from a few microns to 100's of microns provide ample opportunity for building devices for life-science applications.[37] They are stiff, essentially without autofluorescence, and can be disposable. Furthermore, they combine well with existing optoelectronics and fiber-coupled lasers and detectors, giving an undeniable advantage over lab-on-a-chip technology.[38,39] Fiber-based biomedical modules used in life sciences are becoming true "Lab-in-a-fiber" technology with the unique potential of one day being used *in vivo*, for their minimally invasive form factor.

Our group has previously used hollow optical fibers to detect, trap, collect, and analyze particles in fluids.[40,41] The system was further developed into a compact all-fiber flow cytometer by assembling silica optical fibers and micro capillaries.[42] It used elasto-inertial microfluidics in the capillaries for particle focusing and an optical fiber for carrying the light to and from the particles. The high-performance all-fiber device is fabricated at a low cost without the need for clean-room facilities. Recently, a method to fabricate channels with arbitrary cross-sectional shapes using fibers was demonstrated to perform live and dead cell separation.[33] Furthermore, it was shown that the fibers can be co-drawn with compatible materials so that conductive domains can be integrated at arbitrary locations along channel walls.[43]

In this work, we present elasto-inertial particle separation with high efficiency followed by particle counting in an integrated all-fiber microfluidic component. The overall configuration of the component is shown in Fig. 1. Central for the overall function is the three different pieces of capillaries fused in the middle of the component, where the sample is mixed with sheath in the first piece, then a separation takes place based on the size in the second, and particle counting in the last one. As a proof-of-principle, a mixture of 10 μm and 1 μm particles are separated in the system. At the inlet, the particles are sheathed by an elasticity enhancer (PEO). As the particles enter the separation chamber, the larger 10 μm particles start to differentially migrate towards the center and can be collected through a central outlet, while the 1 μm particles exit through a side outlet. The 10 μm are routed through another all-fiber component for counting. A blue laser at 450 nm is used to illuminate the incoming fluorescent particles with the light guided in the core of a double-clad fiber for counting. An impressive separation efficiency of 100% is achieved for the 10 μm particles followed by counting the separated particles at a throughput of 1400 particles per min. The presented work shows that fiber optic technology provides a promising platform to build modular, flexible, and efficient optofluidic systems, which may find several applications in biology and medicine, including in cancer research.

Results and discussion

Using polyethylene oxide (PEO) as an elasticity enhancer, we have previously reported elasto-inertial based particle focusing in circular capillaries at high Reynolds numbers.[42] Based on our previous work,[42] in the current work we settled for a PEO concentration of 500 ppm both for the sheath and the sample throughout the experiments, while different flow rates were tested. Various separation channel lengths and

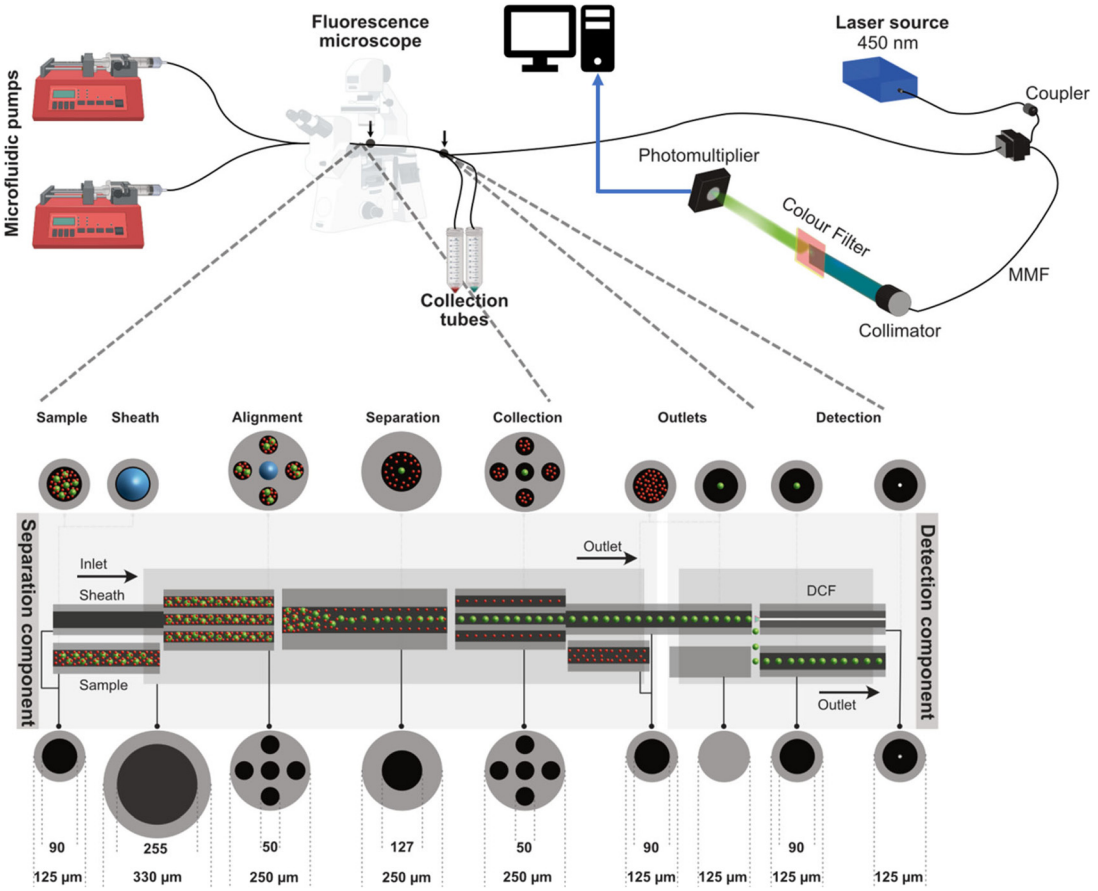

Fig. 1 The overall concept of "lab-in-a-fiber" and experimental setup for separating particles followed by counting. Using an all-fiber separation component, the particles are first sheathed to the side walls followed by a size specific elasto-inertial migration of the larger particles towards the centerline for efficient separation through a central outlet. The separated particles exit the component in two distinct capillaries and the larger fluorescent particles are counted using the light guided in the core of a double-clad fiber.

flow rates of the fluids in the all-fiber separation component (see "Methods" section) were investigated for achieving high separation efficiency. First, we investigated the length of the separation channel for different-sized particles. A 10 cm long 127/250 μm capillary (inner diameter 127 μm/outer diameter 250 μm) was used to evaluate the length dependence. We used four different particle sizes (15, 10, 5, and 1 μm) to study the behavior of their migration with focusing length. Using a sheath flow (PEO, 500 PPM), the particles were initially pushed toward the outer wall and the migration was analyzed. The flow rate of the sample was 10 μL min^{-1} and the sheath was 40 μL min^{-1}. We took fluorescent images of the capillary at the entrance and then at 1, 2, 3, 4, and 5 cm. The results are shown in Fig. 2. The particle migration in capillary depends on size, resulting in faster migration to the center for the larger particles, compared to the smaller particles. The larger 15 μm particle migrated fully to the center of the capillary in 2 cm, whereas the 10 μm particle converged to the center in 3 cm, and the 5 μm particles did not migrate to the center within the 5 cm length monitored. The 1 μm particles stay unfocussed within the 5 cm length. As can be observed, while the combined effect of inertia and elasticity are important, elastic effects gain upper hand at the given PEO concentration of 500 ppm and force the larger particles to the channel center. The size-dependent migration is based on competitive effects of inertia and elasticity, where the lift forces (F_L) push the large particles towards the "Segré-Silberberg annulus" centered at 0.3 times the diameter[27] and the elastic forces (F_E) towards the center. By carefully choosing the channel dimension, length, and flow condition, it is possible to tune the position of a particle between the Segre–Silberberg annulus and the channel center (see the position of the 5 μm and 15 μm particles in Fig. 2). Furthermore, we observed a weak oscillatory behavior around the focusing position. A possible explanation for this is the distorted first normal stress difference that builds up around the particle, leading to an oscillatory stretching around its surface. The interested reader is referred to the work by Banerjee[43] for further analysis of the different migration dynamics leading to the oscillatory behavior of particles in circular channels in weak fluid elastic flows. While more work is needed to fully elucidate the observation of weak oscillatory behavior, there is a huge potential to exploit the strict size-dependent migration of particles for high-resolution separation applications, which has been the focus of the current work. In this respect, the diameter of the

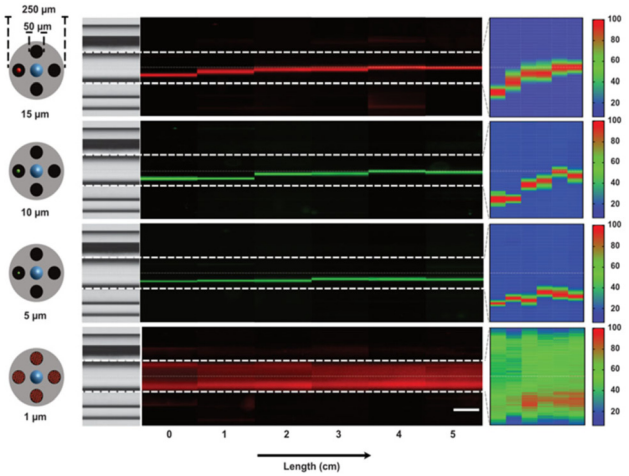

Fig. 2 Fluorescent images of the separation channel taken from the entrance up to 5 cm at an interval of 1 cm for identifying the migratory behavior of particles. The flow rate s are 10 μL min^{-1} for sample and 40 μL min^{-1} for sheath. Larger particles enter the separation capillary pre-focused whereas the 1 μm particle enters from all four holes of the 5-hole capillary. The 15 μm particle at the top migrates to the center of the capillary within 3 cm from the entrance whereas the 1 μm particle remains unfocussed within 5 cm.

central hole of the 5-hole fiber is 50 μm which gives us a tolerance limit of about ±20 μm from the center for collecting the particles migrating towards the center into a separate outlet (see Fig. S1† for schematic illustration of the separation component).

As proof of principle for separation application, we fabricated an all-fiber separation component for 10 and 1 μm particles. The length and diameter of the capillary channel were chosen such that the 10 μm particle has enough length to migrate towards the center and be collected *via* the center hole of the 5-hole capillary at the outlet. The details of the channel layout and fabrication are summarized in Fig. S1.† Initially, we tested the flow rate that allowed the sample to flow from all four holes of the sample inlet capillary and found that 40 μL min^{-1} was sufficient. Following, we tested the total flow rate we could flow with maintained migration of the larger 10 μm particles towards the center and found that the migration was largely independent of the flow rate s (Fig. S2†).

Fig. 3 shows one such image at a total flow rate of 160 μl min^{-1} (40 μL min^{-1} for the sample and 120 μL min^{-1} for the sheath). The larger 10 μm particles are migrating toward the center while the smaller 1 μm particles remained close to the walls. At the given high volumetric flow rate, while migrating from the outer wall, the 10 μm are more spread around the center line. This is mainly due to the influence of dominant lift forces over the viscous forces. A way to improve the focus at the center line involves the combination of the following: increase the migration channel length, reduce the overall flow rate (reduce Re), or increase the PEO concentration (increase Wi). To limit the overall resistance of the system to pressure, the separation length was kept at 3 cm. To allow the 10 μm particles to fully migrate and focus at the center line, we reduced the flow rate (reducing the Re) and maintained the PEO concentration at 500 PPM. Experimentally, we found that a sample flow rate of 10 μL min^{-1} and a sheath flow rate of 40 μL min^{-1} were optimal for the efficient separation of the particles (Fig. 4). Fig. 4A and B show the fluorescent images of the separation component at the end of the separation channel for the 1 μm (red) and 10 μm (green) fluorescent particles. The 10 μm particles enter the central hole of the 5-hole capillary as can be seen in Fig. 4B. Moreover, we see three distinct red lines for the 1 μm particle, indicative of the fact that the particles remain at the same transverse position as they were entering the channel. To examine the particle distribution at the end of the separation capillary, the intensity of the light along the diameter is plotted in Fig. 4C. For the 10 μm particles only one central peak appears, at the center of the migration

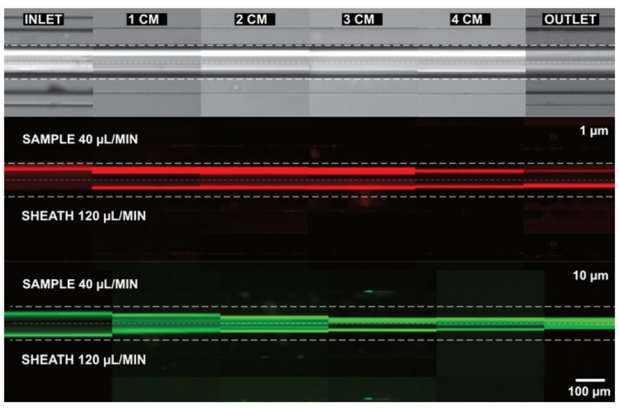

Fig. 3 Fluorescent images of the separation capillary at locations 0 to 5 cm showing the streamlines of the 1 (red) and 10 μm (green) particles. The larger 10 μm particles migrate towards the center while the smaller 1 μm particles remained close to the walls. The flow rate was 40 μL min^{-1} for sample and 120 μL min^{-1} for sheath.

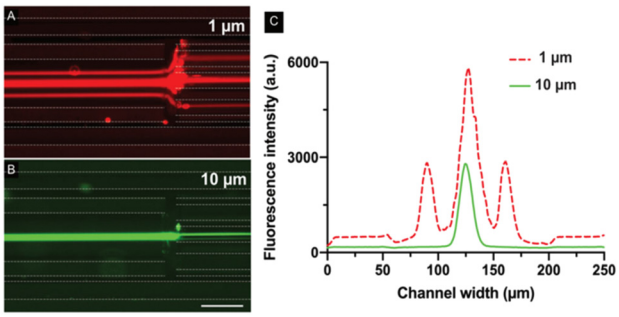

Fig. 4 A) Fluorescent image taken at the end of the separation capillary where the 1 μm red particles are separated from the center and enter the outer four holes of the 5-hole exit capillary, B) fluorescent image of the same where the 10 μm green fluorescent particles are focused to the center and enter the central hole of 5-hole capillary. C) Normalized intensity graph of the cross-section at the end of the separation capillary showing focusing of the 10 μm particles (green). The flow rate s are 10 μL min^{-1} for sample and 40 μL min^{-1} for sheath.

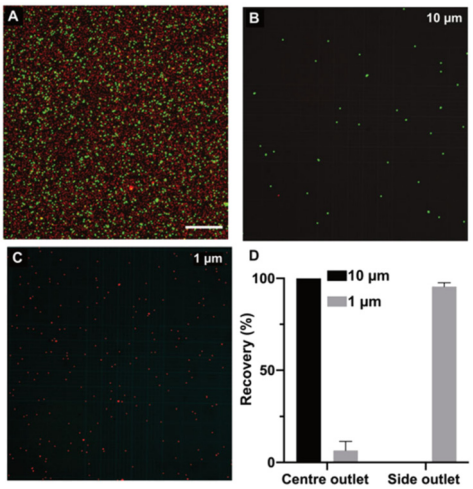

Fig. 5 Analysis of separation efficiency of 1 and 10 μm particles. A) Fluorescent images of 1 (red) and 10 (green) μm particles before separation, B and C) fluorescent images after processing the sample through the separation device. D) Separation efficiency analyzed using a hemocytometer. The graph shows a 100% separation of 10 μm particle and 97% of 1 μm particles.

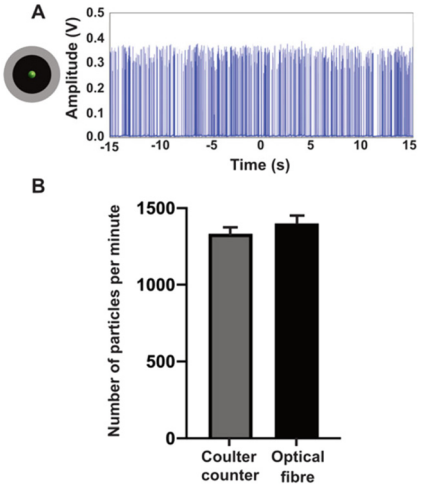

Fig. 6 A) Temporal trace showing the pulse train where each pulse corresponds to one 10 μm particle counted in the all-fiber cytometer device after separation in an all-fiber separation component. The total flow rate was 80 μL min^{-1} (sheath: 40 μL min^{-1} and sample: 40 μL min^{-1}). B) Particle counting results, counted with Coulter counter and the fiber component (n = 5).

capillary, while for the 1 μm particles, there is a large central peak and two smaller peaks on either side. The higher intensity at the center reflects the fact that the upper and lower outlet holes are aligned to produce the higher fluorescence intensity compared to the side outlet holes for the 1 μm particles.

To quantify the separation efficiency, the output was collected at the outlets of the component and analyzed. Fig. 5 shows the fluorescent image taken under a microscope of the 10 and 1 μm particles before (Fig. 5A) and after the separation (Fig. 5B and C). The samples collected at the center hole of the 5-hole capillary primarily contains all the 10 μm particle and very few 1 μm particles. The collected sample from the outer 4 holes of the 5-hole fiber only shows 1 μm particles. The results showed 100% separation of 10 μm particles and 97% of 1 μm particles as can be seen in the bar chart of Fig. 5D. To the best of our knowledge, this is first time a circular cross-section has been used to differential focus and separate particles. While more work is needed to compare the circular cross-section geometry with rectangular cross-section, we speculate that circular cross-section would be more efficient for separation applications due to symmetry since in the circular cross section the first normal stress difference is uniform in the azimuthal direction, which is not the case in rectangular cross sections.

After the separation of 10 μm particles, the sample was routed to a fiber-optic particle-counting device connected to the separation component, as shown in Fig. 1. The particle-counting fiber-optic device is similar to the one used in ref. 42. A blue laser at 450 nm is used to illuminate the incoming fluorescent particles with the light guided in the core of a double-clad fiber. Fluorescence from the particles is collected in the inner cladding of the double-clad fiber and guided to the detector end of the fiber where the signal is filtered through a dichroic filter that only allows green fluorescence light to pass through. The green light is detected using a silicon photomultiplier (SiPM) and the temporal trace is collected using an oscilloscope and analyzed in a PC. The separated 10 μm green particles are counted using the all-fiber component before they are collected in an Eppendorf. After the collection of fluorescent particles from the outlets, the 10 μm particles were also counted using the hemacytometer. Fig. 6A shows the time domain trace for a time window of 30 s of the fluorescence signals collected from the all-fiber flow cytometer device. In this measurement, we used a flow rate of 40 μL min^{-1} for the sheath and 40 μL min^{-1} for the sample. Each pulse in the time trace corresponds to one fluorescent 10 μm particle. We consider each pulse above 0.1 V as a particle and counted 716 particles in 30 s. The coefficient of variation (CV) in the amplitudes of the fluorescence signals is 10%. To verify the number of particles counted using the all-fiber component we collected particles for three minutes and then used a coulter counter to count the number of particles in Eppendorf. We collected five samples to obtain the average number of particles collected per minute (Fig. 6B). With the all-fiber component the average count was 1400 particles per min.

A flow rate of 10 μL min^{-1} for the sample and 40 μL min^{-1} for the sheath showed varying amplitudes of the pulse train (see Fig. S3†). The variation in the amplitude is due to weak particle focusing in the counting capillary. However, with an optimized flow rate of 40 μL min^{-1} for the sample and 40 μL min^{-1} for the sheath, we got better focusing of the 10 μm particle (see Fig. 6) albeit with a lower separation efficiency compared to the flow rate of 10 μL min^{-1} for the sample and 40 μL min^{-1} for the sheath (see Fig. 5).

In this proof-of-principle demonstration, we sorted and analyzed particles at a throughput of ~1400 particles per min. At present, the high resistance of the integrated device prevents higher flow rate s. We believe by optimizing the total component length, increasing the capillary dimension, and using a high-pressure pump we can achieve significantly higher throughputs. We have previously reported focusing and counting at a throughput of ~2500 particles per s using similar fiber components.[42] Another important aspect is related to separation resolution. In this proof of principle, we demonstrated high separation efficiency between 10 μm and 1 μm particle to imitate blood cells and bacteria. However, using elasto-inertial microfluidics it is possible to separate particles at 1–2 μm resolution.[20,26] By finetuning the capillary dimensions and flow conditions, we anticipate efficient separation for lower-size ratio mixtures using the all-fiber component. For instance, we showed size-based differential migration for 15 μm, 10 μm, and 5 μm particles in Fig. 2. By carefully optimizing the channel length and flow rate, higher separation resolution can be obtained in the system.

In summary, an all-fiber separation component capable of sorting micron-sized particles based on size has been presented. In this work, for the first time, we demonstrated high throughput elasto-inertial particle separation in circular channel cross-sections. Furthermore, counting of the separated particles in a single-continuous integrated fiber platform is demonstrated. The low-cost all-fiber device is fabricated without the need for clean-room facilities and can be assembled in versatile combinations for different functionalities. Here we demonstrate powerful size-based passive particle separation, but with few modifications, the versatile lab-in-a-fiber platform could be combined with other techniques including acoustics and magnetophoretics. The integrated all-silica-fiber separation and counting device presented above combines elasto-inertial microfluidics with optical fibers and capillaries and is poised to open new avenues in 'Lab-in-a-fiber' technology for medical diagnostics application. We anticipate that this low-cost platform can contribute to the development of next-generation point-of-care flow cytometers with integrated sample preparation capabilities for blood-based diagnostic applications.

Methods

Experimental setup

The experimental setup for the separation of particles based on size is shown in Fig. 1 and detailed fabrication steps are shown in Fig. S1† along with the schematic of the separation component. The all-fiber separation component has two inlets, one for feeding pure visco-elastic fluid (sheath) and the other carrying the sample (same visco-elastic fluid mixed with particles). Two microfluidic pumps are used to infuse the sheath and the sample into the separation component. In the current experiment, an aqueous fluorescent microsphere suspension with 10 μm (green) and 1 μm (red) was used.

When in operation, a fluorescence microscope can be used to image the streamlines of the fluorescent particles inside the fiber capillary to distinguish the particles. The fluorescence microscope uses a Fluorescein isothiocyanate (FITC) filter cube for the 10 μm fluorescent particles with excitation/emission peaks of 468/508 nm (Green) and a tetramethylrhodamine (TRITC) filter cube for the 1 μm fluorescent particles with excitation/emission peaks of 542/612 nm (Red). The microscope images were taken using a motorized Nikon Ti-Eclipse inverted microscope coupled with a Lumencor SOLA light engine as the excitation source. The images were processed and analyzed using the software ImageJ (NIH, MD, USA).

The sheath and sample are fed into the all-fiber separation component using a mid-pressure syringe pump neMESYS, Cetoni. Two syringes of 25 mL are used to pump the fluids into the separation component. The flow rate s for both the sheath and the sample are controlled independently using neMESYS user interface software. The separation component has two outlets, and the separated particles are collected in two different Eppendorfs for further analysis, or flow into additional all-fiber devices, such as a flow cytometer.

Design and fabrication of all-fiber separation component

A schematic diagram of the separation component is shown in Fig. 1. It uses an assembly of four different silica fiber capillaries, the cross-sections and dimensions of which are shown in Fig. 1. All inlets and outlets consist of capillaries with 90 μm inner diameter and 125 μm outer diameter (90/125 μm). Separation takes place in a 127/250 μm separation channel, where the mixture of particles flows with the viscoelastic fluid, as shown in Fig. 1. The input mixture is fed to the separation channel through a short piece of 5-hole fiber of length 0.5 mm. The central hole of the 5-hole fiber carries only the sheath and the outer four holes carry the mixture of particles. This is accomplished by splicing one of the 90/125 μm capillaries to the central hole of the 5-hole fiber leaving room for the mixture to enter from the outer holes. Part of the structure is encased in a housing capillary with dimensions 250/330 μm. At the output, a similar arrangement with a 5-hole fiber with a central hole spliced to a 90/125 μm capillary is made to collect the separated particles. This 5-hole fiber guarantees that the central collection capillary is aligned with the large, focused particles, and the four outer holes provide low resistance flow for the collection of the smaller particles. The gap between the end of the separation channel and the 5-hole fiber is only 40 μm so that the particles do not deviate significantly from the path. UV-curing glue is used to seal the housing capillary at both ends, preventing leakage. To reduce the clogging of particles inside the fiber device we treated the inside of the entire component with a hydrophobic liquid called "Sigmacote" which is a siliconizing reagent (Sigma-Aldrich SL2-25ML) for glass.

After separation by size, the identification by fluorescence and counting of the 10 μm green particles is carried out. An all-fiber cytometer like the one reported in ref. 42. was built and integrated with the separation component as shown in Fig. 1 labeled detection part. The all-fiber cytometer has a 56/125 μm input capillary where particle focusing takes place and a 90/125 μm output capillary to remove particles after counting. It is fabricated by aligning a double-clad fiber to the input capillary. This fiber provides laser excitation from the 9 μm central core and collects back-scattering and fluorescence light in the inner cladding. Besides the input and output capillaries and the double-clad fiber, the device incorporates a piece of dummy fiber used for simplifying the alignment. An external 250/330 μm housing capillary holds the assembly together as shown in Fig. 1.

Elasto-inertial microfluidic setup

The viscoelastic (non-Newtonian) fluid used in this work was prepared using the polymer polyethylene oxide (PEO) with an average molecular weight (M_v) of 2000 000 (Sigma-Aldrich). Powdered PEO was weighed and added directly to a freshly prepared 1× phosphate buffer saline (PBS) solution. The mixture was left in a magnetic stirrer overnight for mixing. The concentration of PEO used in the experiment was 500 PPM.

Conflicts of interest

There are no conflicts to declare.

Acknowledgements

This work was supported with funds provided by Office of Naval Research Global (N62909-20-1-2033), Swedish Research Council (VR 2021-05861) and Knut and Alice Wallenberg Foundation (KAW 2016-0104).

References

1 P. Sajeesh and A. K. Sen, *Microfluid. Nanofluid.*, 2014, **17**, 1–52.
2 D. Huh, W. Gu, Y. Kamotani, J. B. Grotberg and S. Takayama, *Physiol. Meas.*, 2005, **26**, R73–R98.
3 K. Bacon, A. Lavoie, B. M. Rao, M. Daniele and S. Menegatti, *Acta Biomater.*, 2020, **112**, 29–51.
4 S. Nagrath, L. V. Sequist, S. Maheswaran, D. W. Bell, D. Irimia, L. Ulkus, M. R. Smith, E. L. Kwak, S. Digumarthy, A. Muzikansky, P. Ryan, U. J. Balis, R. G. Tompkins, D. A. Haber and M. Toner, *Nature*, 2007, **450**, 1235–1239.
5 S. L. Stott, C. H. Hsu, D. I. Tsukrov, M. Yu, D. T. Miyamoto, B. A. Waltman, S. Michael Rothenberg, A. M. Shah, M. E. Smas, G. K. Korir, F. P. Floyd, A. J. Gilman, J. B. Lord, D. Winokur, S. Springer, D. Irimia, S. Nagrath, L. V. Sequist, R. J. Lee, K. J. Isselbacher, S. Maheswaran, D. A. Haber and M. Toner, *Proc. Natl. Acad. Sci. U. S. A.*, 2010, **107**(43), 18392–18399.
6 P. Liu, P. Jonkheijm, L. W. M. M. Terstappen and M. Stevens, *Cancers*, 2020, **12**, 3525.
7 D. Antolovic, L. Galindo, A. Carstens, N. Rahbari, M. W. Büchler, J. Weitz and M. Koch, *BMC Biotechnol.*, 2017, **6**(2), 235–242.
8 N. Pamme and A. Manz, *Anal. Chem.*, 2004, **76**, 7250–7256.
9 S. Karthick, P. N. Pradeep, P. Kanchana and A. K. Sen, *Lab Chip*, 2018, **18**, 3802–3813.
10 F. Olm, L. Panse, J. H. Dykes, D. Bexell, T. Laurell and S. Scheding, *Stem Cell Res. Ther.*, 2021, **12**, 542.
11 M. Wu, K. Chen, S. Yang, Z. Wang, P. H. Huang, J. Mai, Z. Y. Li and T. J. Huang, *Lab Chip*, 2018, **18**, 3003–3010.
12 T. Laurell, F. Petersson and A. Nilsson, *Chem. Soc. Rev.*, 2007, **36**, 492–506.
13 B. D. Ho, J. P. Beech and J. O. Tegenfeldt, *Micromachines*, 2021, **12**(1), DOI: **10.3390/mi12010030**.
14 N. Tottori and T. Nisisako, *Lab Chip*, 2020, **20**, 1999–2008.
15 L. R. Huang, E. C. Cox, R. H. Austin and J. C. Sturm, *Science*, 2004, **304**(5673), 987.
16 Z. Zhou, Y. Chen, S. Zhu, L. Liu, Z. Ni and N. Xiang, *Analyst*, 2021, **146**, 6064–6083.
17 M. E. Warkiani, B. L. Khoo, D. S. W. Tan, A. A. S. Bhagat, W. T. Lim, Y. S. Yap, S. C. Lee, R. A. Soo, J. Han and C. T. Lim, *Analyst*, 2014, **139**, 3245–3255.
18 S. S. Kuntaegowdanahalli, A. A. S. Bhagat, G. Kumar and I. Papautsky, *Lab Chip*, 2009, **9**, 2973–2980.
19 J. M. Martel and M. Toner, *Annu. Rev. Biomed. Eng.*, 2014, **16**, 371–396.
20 M. A. Faridi, H. Ramachandraiah, I. Banerjee, S. Ardabili, S. Zelenin and A. Russom, *J. Nanobiotechnol.*, 2021, **12**(3), 257.
21 M. A. Raoufi, A. Mashhadian, H. Niazmand, M. Asadnia, A. Razmjou and M. E. Warkiani, *Biomicrofluidics*, 2019, **13**(3), 034103.
22 S. Yang, J. Y. Kim, S. J. Lee, S. S. Lee and J. M. Kim, *Lab Chip*, 2011, **11**, 266–273.
23 D. Yuan, J. Zhang, S. Yan, C. Pan, G. Alici, N. T. Nguyen and W. H. Li, in *Seventh International Symposium on Precision Mechanical Measurements*, 2016, vol. 9903.
24 Y. Zhou, Z. Ma and Y. Ai, *Lab Chip*, 2020, **20**, 568–581.
25 T. Kumar, H. Ramachandraiah, S. N. Iyengar, I. Banerjee, G. Mårtensson and A. Russom, *Sci. Rep.*, 2021, **11**, 8467.
26 S. Narayana Iyengar, T. Kumar, G. Mårtensson and A. Russom, *Electrophoresis*, 2021, **42**(23), 2538–2551.
27 G. Segré and A. Silberberg, *Nature*, 1961, **189**(4760), 209–210.
28 D. Di Carlo, D. Irimia, R. G. Tompkins and M. Toner, *Proc. Natl. Acad. Sci. U. S. A.*, 2007, **104**(48), 18892–18897.
29 A. Russom, A. K. Gupta, S. Nagrath, D. Di Carlo, J. F. Edd and M. Toner, *New J. Phys.*, 2009, **11**, 075025.
30 S.-Y. Yang, S.-K. Hsiung, Y.-C. Hung, C.-M. Chang, T.-L. Liao and G.-B. Lee, *Meas. Sci. Technol.*, 2006, **17**, 2001–2009.

31 R. Nasiri, A. Shamloo, S. Ahadian, L. Amirifar, J. Akbari, M. J. Goudie, K. J. Lee, N. Ashammakhi, M. R. Dokmeci, D. Di Carlo and A. Khademhosseini, *Small*, 2020, **16**, 2000171.
32 W. Al-Faqheri, T. H. G. Thio, M. A. Qasaimeh, A. Dietzel, M. Madou and A. Al-Halhouli, *Microfluid. Nanofluid.*, 2017, **21**, 1–23.
33 B. Hayes, C. Murphy, A. Crawley and R. O'Kennedy, *Diagnostics*, 2018, **8**(2), 39.
34 C. Monat, P. Domachuk and B. J. Eggleton, *Nat. Photonics*, 2007, **1**, 106–114.
35 A. Ricciardi, A. Crescitelli, P. Vaiano, G. Quero, M. Consales, M. Pisco, E. Esposito and A. Cusano, *Analyst*, 2015, **140**, 8068–8079.
36 R. Yuan, J. Lee, H. W. Su, E. Levy, T. Khudiyev, J. Voldman and Y. Fink, *Proc. Natl. Acad. Sci. U. S. A.*, 2018, **115**, E10830–E10838.
37 M. Serhatlioglu, E. A. Jensen, M. Niora, A. T. Hansen, C. Friberg Nielsen, M. M. Theresia Jansman, L. Hosta-Rigau, M. H. Dziegiel, K. Berg-Sørensen, I. D. Hickson and A. Kristensen, *Optical Trapping and Optical Micromanipulation XIX*, 2022, p. 9.
38 S. Tabassum and R. Kumar, *Adv. Mater. Technol.*, 2020, **5**, 1900792.
39 J. Li, H. Ebendorff-Heidepriem, B. C. Gibson, A. D. Greentree, M. R. Hutchinson, P. Jia, R. Kostecki, G. Liu, A. Orth, M. Ploschner, E. P. Schartner, S. C. Warren-Smith, K. Zhang, G. Tsiminis and E. M. Goldys, *APL Photonics*, 2018, **3**, 100902.
40 A. Sudirman, S. Etcheverry, M. Stjernström, F. Laurell, W. Margulis, O. Lazcka, F. J. Del Campo, F. X. Muñoz, D. A. Veal, D. Deere, B. Ferrari, J. Piper, P. V Attfield, L. Yang, Y. Zhou, S. Zhu, T. Huang, L. Wu and X. Yan, *Opt. Express*, 2014, **22**, 21480–21487.
41 S. Etcheverry, A. Russom, F. Laurell and W. Margulis, *Opt. Express*, 2017, 33657–33663.
42 S. Etcheverry, A. Faridi, H. Ramachandraiah, T. Kumar, W. Margulis, F. Laurell and A. Russom, *Sci. Rep.*, 2017, **7**, 5628.
43 I. Banerjee, M. E. Rosti, T. Kumar, L. Brandt and A. Russom, *Meccanica*, 2021, **56**, 1739–1749.